

Sandra Tolnai, Bernhard Englitz, Jonathan Scholbach, Jürgen Jost and Rudolf Rübsamen

J Neurophysiol 102:1206-1217, 2009. First published Jun 10, 2009; doi:10.1152/jn.00275.2009

You might find this additional information useful...

Supplemental material for this article can be found at:

<http://jn.physiology.org/cgi/content/full/00275.2009/DC1>

This article cites 51 articles, 28 of which you can access free at:

<http://jn.physiology.org/cgi/content/full/102/2/1206#BIBL>

Updated information and services including high-resolution figures, can be found at:

<http://jn.physiology.org/cgi/content/full/102/2/1206>

Additional material and information about *Journal of Neurophysiology* can be found at:

<http://www.the-aps.org/publications/jn>

This information is current as of August 2, 2009 .

Spike Transmission Delay at the Calyx of Held In Vivo: Rate Dependence, Phenomenological Modeling, and Relevance for Sound Localization

Sandra Tolnai,^{1,*} Bernhard Englitz,^{1,2,*} Jonathan Scholbach,³ Jürgen Jost,^{2,3} and Rudolf Rübsamen¹

¹Institute of Biology II and ³Institute for Mathematics, University of Leipzig; and ²Max Planck Institute for Mathematics in the Sciences, Leipzig, Germany

Submitted 27 March 2009; accepted in final form 9 June 2009

Tolnai S, Englitz B, Scholbach J, Jost J, Rübsamen R. Spike transmission delay at the calyx of Held in vivo: rate dependence, phenomenological modeling, and relevance for sound localization. *J Neurophysiol* 102: 1206–1217, 2009. First published June 10, 2009; doi:10.1152/jn.00275.2009. Transmission at central synapses exhibits rapid changes in response amplitude under different patterns of stimulation. Whether the delay associated with the transmission of action potentials is similarly modifiable is important for temporally precise computations. We address this question at the calyx of Held of the medial nucleus of the trapezoid body (MNTB) in Mongolian gerbils in vivo using extracellular recordings. Here the pre- and postsynaptic activity can be observed simultaneously, allowing the definition of an action potential transmission delay (ATD) from the pre- to the postsynaptic side. We find the ATD to increase as a function of spike rate (10–40%). The temporal dynamics of the ATD increase exhibit an exponential shape with activity-dependent time constants (~15–25 ms). Recovery dynamics of ATD were mono- (20–70 ms) or biexponential with fast (3–20 ms) and slow time constants (50–500 ms). Using a phenomenological model to capture ATD dynamics, we estimated $\Delta\text{ATD} = 5\text{--}30 \mu\text{s}$ per transmitted action potential. Using vocalizations and cage noise stimuli, we confirm that substantial changes in ATD occur in natural situations. Because the ATD changes cover the behaviorally relevant range of interaural time differences in gerbils, these results could provide constraints for models of sound localization.

INTRODUCTION

Synaptic transmission lies at the heart of neural information processing. Its properties define the efficacy and timing of interaction between neurons and thus substantially shape network dynamics. Most studies of synaptic transmission have focused on the efficacy of synaptic transmission and its changes under trains of stimulation (Schneggenburger and Forsythe 2006; von Gersdorff and Borst 2002), i.e., different forms of synaptic depression and facilitation. Investigations of the timing of synaptic transmission have, however, been scarce (for review, see Lin and Faber 2002). Synaptic transmission at chemical synapses has long been known to be noninstantaneous, introducing delays on the order of a millisecond (Katz and Miledi 1965). If this delay was invariant, its influence on processing in neural networks might be assumed to be trivial. Recently, however, a number of studies indicated that this delay changes as a function of previous activity of the synapse. Such changes could have profound influences on network dynamics in the context of time codes or spike-time-dependent plasticity where temporally precise integration of spikes is required.

Early studies of the delay in synaptic transmission focused on the neuromuscular junction (Barrett and Stevens 1972; Katz and Miledi 1965) and found that the synaptic delay was not systematically changed by activity. Later studies at central synapses such as the ones formed by the Mauthner cell (Waldeck et al. 2000) and the calyx of Held (Hennig et al. 2008; Wu and Borst 1999) indicated that here the synaptic delay could change under certain stimulation conditions. The most detailed study (Fedchyshyn and Wang 2007) dissected the delay into its axonal, pre- and postsynaptic components and reported pronounced increases during repetitive stimulation at the calyx of Held.

The calyces of Held are exceptionally large synaptic terminals in the medial nucleus of the trapezoid body (MNTB) (Held 1893; Morest 1968) that provide temporally precise, glycinergic inhibition to the brain stem nuclei involved in sound localization, the medial and lateral superior olives (Brand et al. 2002; Moore and Caspary 1983). The calyx' size allows simultaneous recordings of pre- and postsynaptic potentials (Borst et al. 1995; Forsythe 1994) and thus the measurement of synaptic delay and action potential transmission delay. Similarly, pre- and postsynaptic activities can be recorded in vivo using extracellular recordings (Guinan and Li 1990; Kopp-Scheinflug et al. 2003) allowing for the measurement of the action potential transmission delay. This provides the rare possibility to study properties of synaptic transmission in vivo.

In the present study, we obtain extracellular recordings from the calyces of Held of anesthetized Mongolian gerbils in vivo under acoustic stimulation and quantify the action potential transmission delay (ATD) corresponding approximately to the time between the presynaptic and the postsynaptic action potential. Similar to a recent in vivo study (McLaughlin et al. 2008), we find robust, firing-rate-dependent changes in ATD. Further, we quantify the onset and offset dynamics of ATD, relevant in biophysical modeling of synaptic transmission. Using a phenomenological model for the ATD change, we obtain increases in ATD per transmission event and tighter estimates for the time constants. Finally, we demonstrate similar changes of ATD in response to natural stimuli, further supporting their relevance for models of sound localization (Brand et al. 2002; Pecka et al. 2008; Zhou et al. 2005).

METHODS

All experimental procedures were approved by the Saxonian District Government, Leipzig. Thirty-two adult pigmented Mongolian gerbils (*Meriones unguiculatus*, aged 2–4 mo, weighing 45–70 g)

* S. Tolnai and B. Englitz contributed equally to this work.

Address for reprint requests and other correspondence: R. Rübsamen, Institute of Biology II, University of Leipzig, Talstr. 33, D-04103 Leipzig, Germany (E-mail: rueb@uni-leipzig.de).

were anesthetized with a xylazine-hydrochloride/ketamine-hydrochloride mixture (Rompun, Bayer, xylazine 0.007 mg/g body wt ip; Ketavet, Upjohn, ketamine 0.18 mg/g body wt ip initial dose). Hourly injections (subcutaneous) of one-third of the initial dose assured a constant level of anesthesia. The skull of the animal was exposed along the midsagittal line, and a metal bolt was glued to the bone on bregma and stabilized with dental cement. Two holes (500 μm diam, midline position and 1,500 μm lateral to the midline) drilled into the occipital bone 2,000–2,300 μm caudal to the lambdoid suture allowed the insertion of a recording electrode and the reference electrode (silver wire, WPI) in the superficial cerebellum. Animals were placed in a sound-attenuated booth (Type 400, Industrial Acoustic Company) on a vibration-isolated table and fixed in a stereotaxic device using the metal bolt. The animal's body temperature was kept at $\sim 37^\circ\text{C}$. The MNTB was approached dorsally with the animal tilted at $4\text{--}10^\circ$ to the midsagittal plane.

Extracellular recording

Stereotaxic coordinates of the MNTB were determined by on-line analysis of acoustically evoked multi-unit activity using low-impedance glass micropipettes (1 M Ω , filled with 3 M KCl, GB150TF-10, Science Products). Single-unit responses, identified by their compound waveform (CW, Fig. 1D), were recorded using high-impedance glass micropipettes (5–15 M Ω). The voltage signal was preamplified (Neuroprobe 1600, A-M Systems), band-pass filtered (0.3–7 kHz) and further amplified (PC1, TDT). Voltage traces were digitized at a sampling rate of 97.7 kHz (RP2.1, TDT) and stored for subsequent analysis.

Acoustic stimulation

Stimulus waveforms were generated at a sampling rate of 97.7 kHz using custom written MATLAB software (Version 7.3, The Mathworks), transferred to a RP2.1 real-time processor, D/A converted and further sent to a custom-made earphone (acoustic transducer: DT 770 pro, Beyerdynamic) for calibrated (i.e., convolved with the inverse impulse response of the speaker) near-field stimulation. Responses to three stimulation paradigms were recorded: 1) pure tones (100 ms duration, 5 ms cosine rise/fall time, 100 ms interstimulus interval) of predefined frequency/intensity combinations (20 frequencies on a logarithmic scale, 10 intensity levels, 3–5 repetitions) resulting in the unit's frequency response area (Fig. 1F), 2) a sequence of 60 pure tones [50 ms duration, 25 repetitions, 10 ms cosine rise, 4 ms cosine fall time, 80 dB SPL, unit's characteristic frequency (CF) with variable interstimulus interval (random 1–500 ms on a quadratic scale) for determining the recovery time of the action potential transmission delay, and 3) two natural sounds, one dominated by low frequencies (gerbil gnawing on cage, 9 s duration, 25 repetitions, band-pass filtered between 500 and 2,000 Hz, Fig. 5A1) and one dominated by high frequencies (gerbil's call when barging into a group of individuals, 5.5 s duration, 25 repetitions, Fig. 5A2).

Data analysis

The recorded voltage traces were analyzed using custom-written MATLAB software. CWs were extracted using typical spike-sorting techniques [triggering at a visually determined level, followed by principal-component analysis for dimensionality reduction and hierarchical clustering (MATLAB function: *clusterdata*) of the representation in the 3 principal components with the largest eigenvalues].

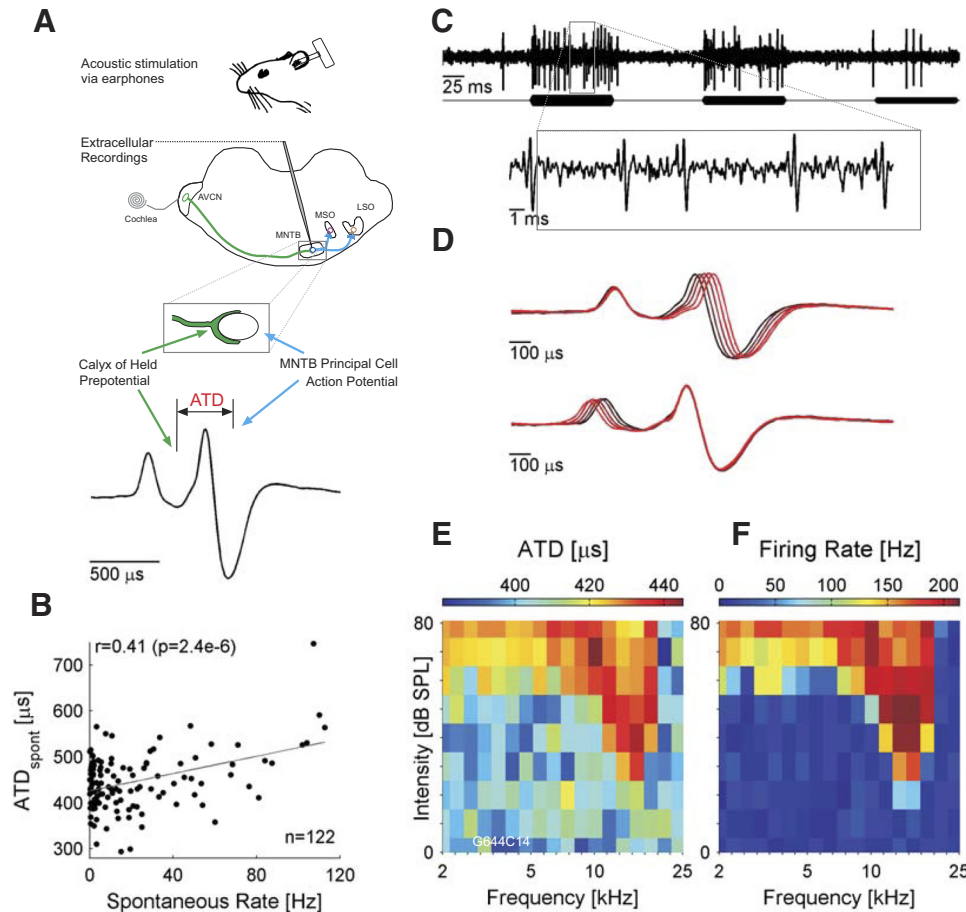


FIG. 1. Measuring the action potential transmission delay (ATD). **A:** extracellular recordings of responses to acoustic stimulations of principal cells of the medial nucleus of the trapezoid body (MNTB) and their presynaptic input, the calyxes of Held in the Mongolian gerbil. Due to the size of the calyx, extracellular recordings resemble complex waveforms that consist of the discharge of the calyx (prepotential) and the action potential (AP) of the principal cell. ATD was measured as the distance between the positive peak amplitudes of prepotential and postsynaptic AP. **B:** ATD measured under silent condition depends on the spontaneous discharge rate of a given MNTB unit. Significantly higher ATD_{spont} are found in units with higher spontaneous rates. **C:** extracellular recording (top) of a unit's response to a sequence of pure tones (bottom, duration: 100 ms, interstimulus interval: 100 ms, stimulus amplitudes in decreasing order, not to scale). **D:** mean complex waveforms of the same unit as in **C** for 5 different ATDs (380–460 μs , black to red) aligned to the prepotential (top) and to the postsynaptic AP (bottom). Individual complex waveforms of ATDs in a 10 μs bin were pooled into each mean complex waveform. **E** and **F:** changes in ATD and firing rate correlate (same unit as in **C**). ATD (**E**) changes as a function of intensity and frequency of the acoustic stimulus and the firing rate (**F**) show a very similar profile.

Units were included if the presynaptic peak $\text{SNR}(\text{PP}) = \max(\text{PP}) / \text{std}(\text{Noise})$ exceeded 3. The ATD was defined as the time between the pre- and the postsynaptic maximum of the CW, comparable to McLaughlin et al. (2008). For each CW, these maxima were determined using a symmetric search radius (size: 1/2 of the ATD in the average CW) around the corresponding maxima from the average CW. Within each search radius the largest local maximum was chosen. For interspike intervals (ISIs) < 2 ms, the following CW was excluded from ATD analysis to exclude interaction effects between CWs (results including all CWs were quite similar; data not shown). Firing rates (FRs) were always based on the entire set of CWs. For an interpretation of the relation between the extracellularly recorded signals and their corresponding underlying intracellular signals, see DISCUSSION.

ATD as a function of FR was analyzed based on the responses to tuning stimuli (see stimulation paradigm 1). Responses were binned according to their FR (25 Hz spacing). For each bin, the average ATD was computed for the CWs in the last 50 ms of the response to exclude adaptation dynamics. The shape of the functional dependence between ATD and FR was assessed by fitting first- and second-order polynomials to the data. Model selection was based on the Bayes Information Criterion (Schwarz 1978).

Onset and recovery dynamics were quantified by fitting mono- and biexponential functions (MATLAB: `nlinfit`) to the respective time courses of ATD. Onset dynamics were determined for each FR bin (described in the preceding text) for the tuning responses. Monoexponential fits described the onset dynamics well, hence, only a single time constant ($\tau_{D,\text{rise}}$) was estimated. Recovery dynamics were determined based on the responses to the variable interstimulus interval stimuli (see stimulation paradigm 2). For each pure tone, the ISI between the last CW elicited by the respective pure tone and the next CW was determined. The ATD of the second CW was then analyzed as a function of ISI. For spontaneously active units, the second CW was not necessarily elicited by the following pure tone. Here the range of ISIs for which ATD could be estimated was limited by the longest occurring ISI. Monoexponential (with time constant $\tau_{D,\text{mono}}$ and amplitude $A_{D,\text{mono}}$) and biexponential ($\tau_{D,\text{fast}}$, $\tau_{D,\text{slow}}$ and $A_{D,\text{fast}}$, $A_{D,\text{slow}}$, respectively) functions were fit to the ATD recovery. Biexponential fits often but not always provided a significantly better explanation of the data. Model selection was again based on Bayes Information Criterion.

Phenomenological model of ATD

To predict individual ATDs and obtain an alternative estimate of the time constants of recovery a simple, dynamical model of the ATD was fitted (MATLAB: `nlinfit`) to the responses of stimulus 2. The model was a one- or two-dimensional (1D or 2D) ordinary differential equation, where each dimension was given by

$$\frac{d\text{ATD}_c(t)}{dt} = -\text{ATD}_c(t)/\tau_{M,c} + \sum_{i=1 \dots N} A_{M,c} \delta(\text{CW}_i - t)$$

and N denotes the number of CWs in a given recording. Each component ATD_c decreases with a respective time constant $\tau_{M,c}$ and increases by the amplitude $A_{M,c}$ (units: $\mu\text{s}/\text{CW}$) for each transmission event CW_i . The entire ATD is then given as $\text{ATD}(t) = \text{ATD}_{\text{fast}}(t) + \text{ATD}_{\text{slow}}(t) + \text{ATD}_{\text{base}}$ for the 2D model and $\text{ATD}(t) = \text{ATD}_{\text{mono}}(t) + \text{ATD}_{\text{base}}$ for the 1D model. See DISCUSSION for an attribution to underlying physiological processes. Several runs of parameter estimation with systematically varied initial values were conducted to avoid local minima in prediction error. In simulations, estimation of parameter values proved to be quite accurate (see Supplementary Material).¹

¹ The online version of this article contains supplemental data.

Noise-induced measurement error

To separate intrinsic variability from noise-induced variability in ATD, the latter was estimated in simulations. For this estimate, one needs to know the influence of the noise on the ATD in terms of their standard deviation (S.D.) and the level of noise at each CW. To address the first point, we added experimentally collected stretches of noise to the average CW (Fig. 4B, left). The S.D. in ATD was then measured for a number of noise levels (1,000 stretches per level of S.D., ~ 10 levels of S.D. per recording). The noise fragments were binned according to their S.D., thus providing a function of the S.D. in ATD as a function of the S.D. of the noise. An example of such a relationship is depicted in Fig. 4B (right). To address the second point, the S.D. of the underlying noise was estimated for each CW by subtracting the temporally aligned, average CW and computing the S.D. of the remaining voltage within 3 ms following the negative peak of the CW. This estimate was validated using simulated recordings (see Supplementary Material). Hence an estimate of the local, noise-induced measurement error for each CW was obtained.

To estimate the quality of the model predictions, the total variance of the sequence of ATDs was decomposed into a part attributable to the measurement error and an intrinsic part: $\sigma_{\text{total}}^2 = \sigma_{\text{meas.noise}}^2 + \sigma_{\text{intrinsic}}^2$. For this decomposition to hold, we need to assume that the measurement errors and the intrinsic changes are independent. While one tries to explain $\sigma_{\text{intrinsic}}^2$, we can estimate and correct for $\sigma_{\text{meas.noise}}^2$. For a given sequence of ATDs the latter ($\hat{\sigma}_{\text{meas.noise}}^2$) was estimated by averaging the local, noise-induced measurement variance over all CWs for each recording, i.e.

$$\hat{\sigma}_{\text{meas.noise}}^2 := \frac{1}{N} \sum_{i=1, \dots, N} \sigma_{\text{meas.noise}}^2(\text{CW}_i)$$

The latter variance at each CW, $\sigma_{\text{meas.noise}}^2(\text{CW}_i)$, was computed from the local error described above. Gaussian kernel regression was used to obtain a smooth estimate over the range of relevant S.D. of the noise (e.g., Fig 4B, right). The variance explained by the model was then normalized by the difference between the total variance and the measurement error variance, i.e., $\sigma_{\text{expl.corr}}^2 = \frac{\sigma_{\text{explained}}^2}{\sigma_{\text{total}}^2 - \hat{\sigma}_{\text{meas.noise}}^2}$, depicted in Fig. 4G.

Because this method assumes fairly constant CWs, recordings were excluded from the analysis of prediction quality, if they exhibited substantial variations in CW size. Those would lead to an overestimate in prediction quality. Further, recordings were excluded if the asymptotic variations in ATD remained $< 20 \mu\text{s}$, in which case the explainable variance is likely to be insignificant compared with the noise variance (see Supplementary Material).

Error bars signify 1 SE unless stated otherwise. Correlation (r) values denote Spearman rank order correlation unless linear correlations were assessed using the Pearson coefficient. For averages, dispersion is indicated as \pm S.D. for means and [25, 75] percentiles for medians.

RESULTS

We analyzed the ATD at the calyx of Held and its activity-dependent changes for 122 principal cells of the MNTB in the anesthetized Mongolian gerbil. ATD was measured as the time between the positive peak amplitudes of the extracellularly recorded CWs, which correspond to the pre- and postsynaptic action potential, respectively (Fig. 1A, see DISCUSSION for more details).

First evidence for a modulation of ATD was obtained from a sequence of acoustic stimulations which induced different firing rates (FRs, Fig. 1C). ATDs collected from the CWs of

these responses differed on the order of $100 \mu\text{s}$ (Fig. 1D). Comparing the ATD for CWs elicited at different FRs indicated that the source of ATD changes has a systematic, activity-dependent component. Further support for this hypothesis came from a comparison of the tuning characteristics of FR and ATD. Tunings based either on ATD (Fig. 1E) or on FR (Fig. 1F) exhibited a remarkably similar dependence on the stimulus' intensity and frequency. Finally, differences in ATD existed already during spontaneous activity ($\text{ATD}_{\text{spont}}$). For spontaneous rates between 0 and 113 Hz (median: 10 [2, 29] Hz, $n = 122$), the $\text{ATD}_{\text{spont}}$ varied between 294 and 748 μs (mean: $443 \pm 63 \mu\text{s}$, $n = 122$) among units. $\text{ATD}_{\text{spont}}$ tended to be larger in units with high spontaneous activity ($r = 0.41$, $P < 0.001$, Fig. 1B).

ATD changes in an activity-dependent manner

To test whether ATD is indeed related to firing activity, we measured the ATD for a range of average FRs induced by acoustic stimulation (Fig. 2A). ATD was estimated as the average ATD reached in the final 50 ms of the response to the stimulus presentation (Fig. 2A2, gray box); FR was calculated for the total length of the stimulus. The use of average FRs differs from the usual *in vitro* paradigm employing "constant-

interval" FRs. We attempted to generate constant-interval FRs using acoustic click trains, yet here the ATDs were obstructed by synchronized potentials of neighboring units. While comparability with *in vitro* studies is hence limited, the presently used average FRs will be closer to naturally occurring spiking patterns. The example in Fig. 2A2 demonstrates that higher FRs entail higher levels of ATD [compare 75 Hz (∇) vs. 275 Hz (\diamond) FR]. Plotting ATD against FR for this unit resulted in a monotonically increasing function: ATD was minimal at $\text{FR} \leq 25$ Hz with 447 μs and increased to 537 μs at 300 Hz (Fig. 2A3). FR-dependent increases of ATD were typical for the vast majority of units (121/122; Fig. 2B, 30 examples). The shape of the dependence of ATD on FR typically appeared linear over a large range, sometimes saturating at the ends of the FR range. The entire sample could be well described by first- or second-order polynomials (Bayes Information Criterion). In 55% of the units (67/122) the increase was better described by a first-order polynomial. The median explained variance of the fit amounted to 98 [96.5, 98.5] percent. In the remaining 45% of units (55/122) the increase in ATD was better fit by a second-order polynomial, capturing saturations for very high FRs or delayed increases for very low FRs in some units. The median explained variance for these units was 96 [93.7, 97.5] percent.

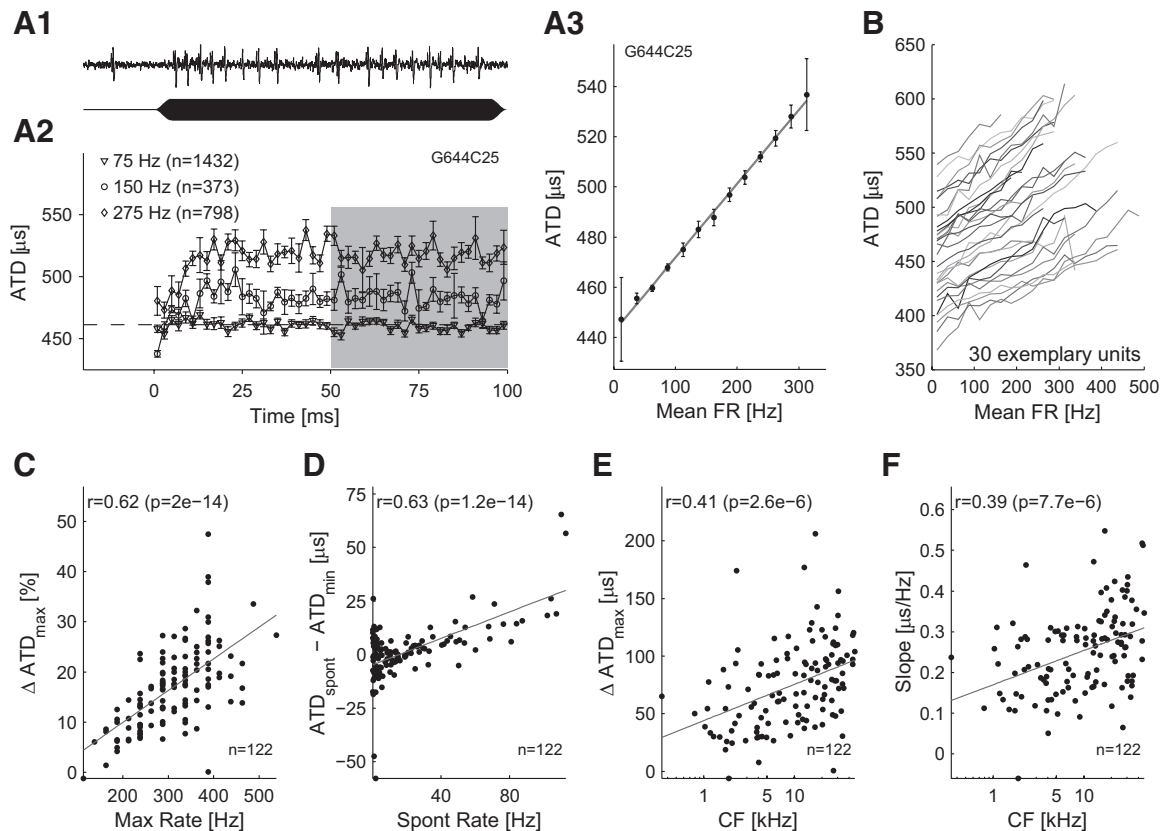


FIG. 2. Magnitude of ATD changes. *A1*: extracellular recording (*top*) of a unit in response to a 100 ms pure tone (*bottom*). *A2*: ATD during acoustic stimulation (0–100 ms). Mean ATDs (time bin: 2 ms) pooled from responses with firing rates (FRs) of 75 Hz (∇), 150 Hz (\circ), and 275 Hz (\diamond). FR is calculated as the mean for the total duration of the stimulus. ATD in silence was 470 μs (---). *A3*: ATD increases with increasing FR [unit G644C25, same as in *A2*, characteristic frequency (CF): 25.7 kHz]. ATD is calculated from the average asymptotic ATD reached during acoustic stimulation (50–100 ms, gray box in *A2*). *B*: ATD vs. FR functions for 30 exemplary units. *C*: in the whole ensemble ($n = 122$), maximal ATD changes (relative to ATD at minimum FR) correspond well to maximal FRs ($r = 0.62$, $P \ll 0.001$). *D*: ATD for spontaneous spikes correlates with spontaneous FR when ATD is referenced to baseline values at the minimal FR of each unit ($r = 0.63$, $P \ll 0.001$). *E* and *F*: both increases in ATD and slopes of ATD vs. FR functions show a significant correlation with CF ($r = 0.41$, $P \ll 0.001$ and $r = 0.39$, $P \ll 0.001$, respectively). These effects can only partly be explained by a correlation between maximal firing rate and CF ($r = 0.19$, $P = 0.03$).

Magnitude of ATD changes

In evaluating the practical significance of the activity-dependent change in ATD, the magnitude of the change is relevant. We measured this change as the difference between ATD at the minimum and maximum FRs of each unit. The average maximum change was $82 \pm 38 \mu\text{s}$, but increases could be as high as $218 \mu\text{s}$ (Fig. 2E). The average increase of ATD was $0.26 \pm 0.11 \mu\text{s}/\text{Hz}$ FR. The maximum ATD changes corresponded to an average relative increase of $19 \pm 9\%$ and depended strongly on the maximum FR reached in single units ($r = 0.62$, $P \ll 0.001$, Fig. 2C). Although $\text{ATD}_{\text{spont}}$ depended on the spontaneous FR of a unit (Fig. 1B), spontaneous FR allowed no prediction about the activity-dependent increases of ATD ($r = 0.02$, $P = 0.83$). However, in spontaneously active units the spontaneous FRs are often far higher than the minimum FRs because certain stimuli can suppress the firing rate below the spontaneous FR. To check whether the ATD is already elevated by spontaneous activity, we compared the $\text{ATD}_{\text{spont}}$ to the ATD at the minimal FR. Consistent with the general activity dependence we found good correlation between these two states ($r = 0.63$, $P \ll 0.001$, Fig. 2D). From this relationship, one would expect that units which have high spontaneous activity only exhibit less of an increase in ATD between their spontaneous and their maximal FR. While the

data are consistent with this expectation ($r = -0.22$, $P = 0.01$, data not shown) and supported by in vitro data (Hermann et al. 2007; p. 817), the correlation is fairly weak due to the difference in maximal FR between the units.

CF (frequency at which units are most sensitive) predicted well the ATD changes and the slope of ATD changes as a function of FR (linear fit, Pearson's correlation coefficient: $r = 0.41$, $P \ll 0.001$ and $r = 0.39$, $P \ll 0.001$, respectively, Fig. 2, E and F). Partly this dependence might be attributable to the correlation between maximum FR and CF ($r = 0.18$, $P = 0.05$, data not shown). In other words, because high CF units tend to have higher maximum FRs higher ATD changes and slopes are more likely to occur. Thus at least in part the observed CF dependence is due to firing properties of the units.

Dynamics of ATD changes

In a time-critical system such as the auditory system, the time course of ATD changes becomes relevant for information processing. Therefore we analyzed the rise of ATD during the initial phase of the response to a stimulus (Fig. 3, A–C) and the recovery of ATD changes (Fig. 3, D–H).

RISE OF ATD INCREASE. As apparent from single unit examples (Figs. 2A2 and 3B) ATD starts increasing with the beginning of

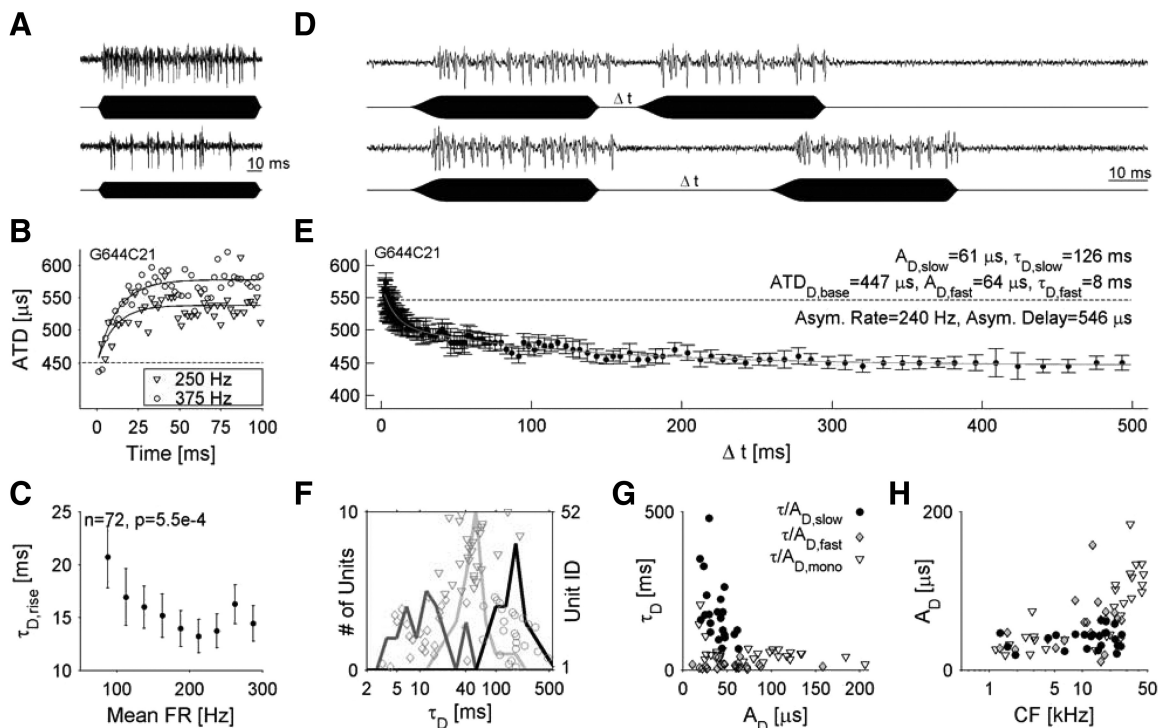


FIG. 3. Dynamics of ATD changes. *A*: the rise dynamics in ATD during acoustic stimulation was induced by presenting pure tones of frequency/intensity combinations that evoked responses of different FRs (*top*: FR = 390 Hz, *bottom*: FR = 130 Hz, unit G644C21, CF: 17.8 kHz). *B*: after stimulus onset, the rise of ATD follows a monoexponential shape (see also Fig. 2A2). In this unit, time constants were 11 ms for FR = 250 Hz (∇) and 20 ms for FR = 375 Hz (\circ). Lines show monoexponential fits. *C*: time constants for the rise of ATD ($\tau_{D,\text{rise}}$) decrease significantly (Friedman test: $P < 0.001$, $n = 72$) with increasing FR. Only FRs for which $\tau_{D,\text{rise}}$ could be reliably estimated for more than half the units are displayed. *D*: the recovery of ATD was investigated by presenting pure tones with interstimulus intervals (Δt) varying between 1 and 500 ms. Recovery values were obtained only from the first CW following the last stimulus. To avoid synchronisation potentials, the stimulus rise time (10 ms) was longer than the fall time (4 ms). *E*: recovery of ATD for the same unit follows a biexponential course decreasing from an asymptotic ATD = 546 μs to an $\text{ATD}_{D,\text{base}} = 447 \mu\text{s}$ with $\tau_{D,\text{fast}} = 8 \text{ ms}$ and $\tau_{D,\text{slow}} = 126 \text{ ms}$. *F*: distribution of mono (∇ , $n = 28$)- and biexponential ($\tau_{D,\text{slow}}$: \circ , $\tau_{D,\text{fast}}$: \diamond , $n = 24$) recovery time constants. Units were sorted according to bi- and monoexponential fits for better visualization. *G*: $\tau_{D,\text{slow}}$ decreases significantly with increasing amplitudes $A_{D,\text{slow}}$ (\circ , $n = 24$, $P < 0.01$). Neither $\tau_{D,\text{fast}}$ (\diamond , $P = 0.7$) nor $\tau_{D,\text{mono}}$ (∇ , $P = 0.15$) showed a similar correlation with the amplitudes. *H*: only $A_{D,\text{mono}}$ showed a significant correlation with the units' CF, while $A_{D,\text{fast}}$ and $A_{D,\text{slow}}$ showed only little dependence (same symbols as in *G*).

the acoustic stimulus (at 0 ms in Figs. 2A3 and 3B) and reaches a plateau as the stimulus continues. Because the increase in ATD is likely to depend on the number of transmission events in a given time span, a common time constant is unlikely to be found across FRs. Therefore time constants were estimated for the rise of ATD ($\tau_{D,rise}$) at a range of FRs using monoexponential fits (lines in Fig. 3B). Reliable estimates for $\tau_{D,rise}$ could be obtained for the whole range of FRs between 75 and 300 Hz for 72 units. Average $\tau_{D,rise}$ ranged from 13 to 21 ms and FR had a significant effect on $\tau_{D,rise}$ (Friedman test, $P < 0.001$, Fig. 3C). At 200 Hz $\tau_{D,rise}$ was significantly lower compared with both 75 and 100 Hz ($P < 0.05$, rank-based post hoc test with Tukey-Cramer correction for multiple tests, MATLAB function: multcompare). The shape of this dependence could be a consequence of the reduction in FR from the onset to the tonic part of the response.

RECOVERY FROM ATD INCREASE. To estimate the recovery dynamics of ATD we probed the ATD at different times after stimulus offset (Δt : 1–500 ms) using a second pure tone (Fig. 3D). In 25/52 units, the recovery of ATD followed a biexponential decrease (Bayes Information Criterion, Fig. 3E). Median time constant for the fast component ($\tau_{D,fast}$) was 11 [7, 18] ms (Fig. 3F, dark gray and \diamond), median time constant for the slow component ($\tau_{D,slow}$) 180 [119, 211] ms (Fig. 3F, black and \circ). Neither $\tau_{D,fast}$ nor $\tau_{D,slow}$ correlated with CF ($P = 0.23$ and $P = 0.75$, respectively). However, $\tau_{D,slow}$ decreased significantly with its amplitude $A_{D,slow}$ (Pearson's correlation coefficient: $r = -0.60$, $P = 0.02$, Fig. 3G, \circ), while $\tau_{D,fast}$ did not correlate with $A_{D,fast}$ (Pearson's correlation coefficient: $P = 0.75$, Fig. 3G, \diamond).

In 27/52 units the recovery of ATD followed a monoexponential decrease with a median time constant of 51 [39, 62] ms (Fig. 3F, light gray and ∇) and thus covered the range between $\tau_{D,fast}$ and $\tau_{D,slow}$ of the biexponential fits. Time constants were neither correlated to CF ($P = 0.13$) nor to $A_{D,mono}$ (Pearson's correlation coefficient: $P = 0.06$, Fig. 3G).

The main difference between units exhibiting a mono- or a biexponential ATD recovery was the spontaneous activity. Units with monoexponential recovery had median spontaneous rates of 26 [13, 67] Hz, compared with only a median of 1 [0.4, 10] Hz for units with biexponential recovery (median significantly different at $P < 0.001$, 2 group Wilcoxon rank sum test). In the former group, due to the high spontaneous activity the ATD could not be measured at large Δt preventing a reliable estimation of the slow component.

Phenomenological model captures ATD changes

In the previous sections, we mostly considered average values of ATD. However, during normal operation, FRs will constantly change and thus preclude any asymptotically attained ATDs. At the same time, the precise temporal sequence of CWs should be determinant for the progression of ATD. We therefore considered the sequence of ATDs for individual CWs without averaging. As a model for the ATD dependence on the sequence of CWs, we chose a simple phenomenological model: for each CW, the ATD is increased by a fixed amount and then decays exponentially afterward. In line with the results from the previous section and Fedchyshyn and Wang (2007), we fitted both a mono- and a biexponentially decaying model (see METHODS).

Figure 4A shows the predicted dynamics in ATD in response to a spike train with realistic interspike intervals: Closely timed CWs increase the ATD to a plateau, which is maintained if the rate stays high. Distributed CWs barely raise the ATD above its baseline duration.

Yet how much of the systematic change in ATD does a given model capture? To answer this question, the quality of the model prediction has to be evaluated against the contributions of noise. The proper assessment of model prediction quality requires estimating the predictable part of the signal, or conversely correcting for the noise-induced, unpredictable part. In the case of ATD measurements, the latter is the temporal jitter caused mainly by voltage noise. To estimate the average temporal jitter, we determined 1) the dependency of the temporal jitter on noise strength and thus 2) the noise strength at each CW. Addressing 1), stretches of voltage noise (collected from nonspiking periods of the response) were added to the average CW (Fig. 4B, left) and the S.D. of the resultant ATDs were measured (Fig. 4B, right). As a function of S.D. of the noise, the temporal jitter in ATD exhibited a monotonically increasing, nonlinear shape (Fig. 4B, right, line fits obtained by Gaussian kernel regression). Addressing 2), we computed the S.D. of the noise in a short (3 ms) window following each CW. Combining 1) and 2) provided local error bounds for the ATD predictions (Fig. 4C) and allowed the proper assessment of model prediction quality based on the explainable variance (see METHODS and Supplementary Material).

An example of the measured ATDs (black dots), the predicted ATDs at each CW (red dots) and the 95% confidence bounds (2 S.D. of temporal jitter, light blue) are shown in Fig. 4C. The model was estimated based on $\sim 20,000$ CWs contained in the recording (25×9 s, in response to the same sequence of tones as in previous section); a single trial is depicted in the top part of C. Because the model predicts the ATD also in between the CWs, the underlying progression in ATD can be visualized (dark blue line).

Next, the properties of the ATD as captured by the model are related to the properties captured by the asymptotic measurements from the previous sections. The ATD model provided a similar estimate for amplitudes of increases ($A_{M,mono}$, $A_{M,fast}$, $A_{M,slow}$) in ATD and time constants of recovery ($\tau_{M,mono}$, $\tau_{M,fast}$, $\tau_{M,slow}$).

First the amplitude of ATD change is considered (Fig. 4D). Rather than the asymptotic increase, the model allows to estimate the change in ATD per event, i.e., the single event increase. For the biexponential model, $A_{M,fast}$ (blue, median: 15.1 [10.6, 20.6] μs) dominates over $A_{M,slow}$ (red, median: 0.66 [0.43, 0.85] μs) and essentially coincides with $A_{M,mono}$ (black, median: 12.7 [9.2, 18.2] μs). This range of values agrees with the single event estimates obtained in vitro at 35°C (Fedchyshyn and Wang 2007; see DISCUSSION for details). However, comparing the quantities measured in Fedchyshyn and Wang (2007) [synaptic delay and excitatory postsynaptic current (EPSC) rise delay] with the presently measured quantity (ATD) is nontrivial because the EPSC rise delay and the postsynaptic contribution to ATD can differ. For the latter, this contribution is the time from the EPSC onset to the onset of the spike, which will often differ from the EPSC rise delay.

Second, the time constants for the mono- and biexponential models are considered (Fig. 4E): again, $\tau_{M,mono}$ (black, median 25.4 [19.5, 33.4] ms) falls in a similar range as $\tau_{M,fast}$ (20.0

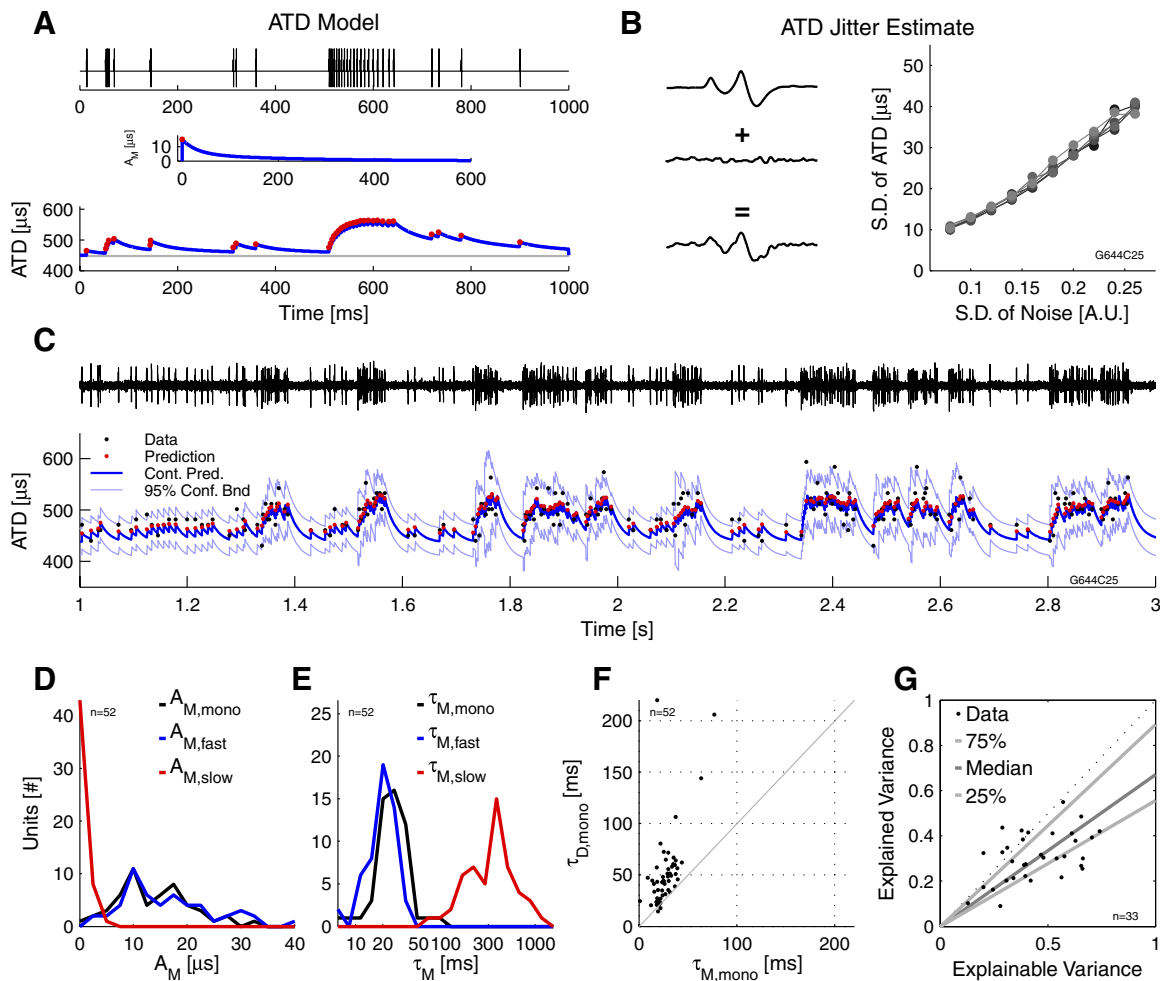


FIG. 4. Phenomenological model of ATD dynamics. Mono- and biexponential dynamical models were fitted to the sequence of ATDs, providing parameter estimates, and the quality of prediction was estimated under noise. **A**: in the model, the ATD is increased by a fixed time Δ ATD per event and then decays mono- or biexponentially (*middle*), resulting in a complex ATD sequence (*bottom*). **B**: estimating the quality of the model requires estimating the influence of the noise on the measured ATD. In simulations, we added noise to the mean CW of each actual recording (*left*). For different noise strengths, ATDs are then changed to different degrees (*right*). Results from 5 recordings of 1 cell are overlaid (different gray levels). **C**: given a recording (*top*) and the measured ATDs (*bottom*, black dots), the dynamical models were fitted using standard nonlinear least squares. The model prediction (dark blue and red dots at the event times) and the estimated 95% confidence bound (light blue, 2^*SD from **B**) demonstrate that after taking measurement errors into account, the model can explain the observed ATDs well. **D**: distribution of estimated single event amplitudes A_M for both the monoexponential ($A_{M,mono}$) and biexponential model ($A_{M,slow}$, $A_{M,fast}$). $A_{M,slow}$ (red) is dominated by $A_{M,fast}$ (blue), which is similar to $A_{M,mono}$ (black). **E**: distribution of estimated τ_M for both the mono- and biexponential model. The $\tau_{M,fast}$ (blue) is slightly lower than $\tau_{M,mono}$ (black), which exhibits a broader distribution, probably due to its low corresponding ATD change. $\tau_{M,fast}$ (red) covers a wide range. **F**: comparison of $\tau_{M,mono}$ (dynamic model) and $\tau_{D,mono}$ (decay from asymptotic). Although results from both methods correlate well, the continuous estimates are more constrained (see also RESULTS). **G**: estimates of the explainable and explained variance, both before (ordinate) and after correction for measurement errors (ordinate rel diagonal). The corrected explained variance had a median (dark gray line) of 67 [56, 91] (light gray lines) percent. A number of cells had to be excluded to reduce underestimation of explainable variance (see Supplementary Material).

[15.1, 25.6] ms). The downward shift of $\tau_{M,fast}$ can be explained by the compensatory effect of the presence of $\tau_{M,slow}$. The latter shows a broad distribution (red, median: 349 [196, 495] ms), probably as a consequence of the small $A_{M,slow}$.

In Fig. 4F, we compared the two different estimates of the time constants. Although the estimates of τ_{fast} correlate well between the two methods ($r = 0.80$), the ATD model estimate ($\tau_{M,mono}$) is systematically lower and tighter constrained than the recovery estimate ($\tau_{D,mono}$). This difference probably rests on the details of the estimation methods: While for the phenomenological model all ATDs can be taken into account, the analysis of $\tau_{D,mono}$ only considers the interstimulus intervals. Hence, the phenomenological model is better constrained but on the other hand could be biased by the distribution of ATDs.

Finally, we assessed the quality of the (biexponential) model prediction (Fig. 4G). For each cell, the explained variance is plotted versus the explainable variance, hence, values around the diagonal indicate prediction which captures the systematic part of the response. The naïve explained variance (median: 31 [24, 40] percent) remains far below the explained variance corrected for variance due to measurement errors (median: 67 [55, 90] percent, solid lines in Fig. 4G). Hence, while there still exists room for improved models of ATD dynamics, the simple phenomenological models tested here already account for 2/3 of the explainable variance. As shown in the Supplementary Material, this value underestimates the explained variance especially for low values in A_M or τ_M (i.e., if intrinsic changes in ATD are dominated by measurement errors). For the depicted unit (Fig. 4C), the bi- (mono-) exponential model

accounted for 96% (95%) of the explainable variance. Results for the monoexponential model were similar (data not shown).

ATD changes also in response to natural stimuli

To check if activity-dependent changes of ATD are present in responses elicited by naturally occurring sounds, we used ambient sounds (Fig. 5A1) and gerbil calls (A2) as acoustic stimuli. The first stimulus had mostly low-frequency content and was used to drive low-CF units; the second stimulus was dominated by high frequencies and was used to drive high-CF units. Units responded to the stimuli with changes in their FRs according to the frequency content and the sound pressures of the stimuli (compare Fig. 5, A and B). As suggested by the results for pure tone stimulations, changes in FR were accompanied by changes in ATD (Fig. 5C, black dots: single trial, red/pink: mean/S.D. of ATD over 25 trials). Both increases and decreases in FR related directly to increases and decreases in ATD (compare Fig. 5, B and C) and could be well captured by the (here biexponential) model's prediction (Fig. 5C, blue line, note that the prediction is for a single, randomly chosen trial). Plotting ATD as a function of instantaneous FR (estimated

over a 24 ms window preceding the CW) resulted in an increasing function (Fig. 5D) resembling the ATD-FR function observed for pure tone stimulations (Fig. 2, B and C). The ATD distributions were fairly broad, indicating that the stimulation with natural stimuli induced a wide range of ATDs (Fig. 5E, black lines). After "de-noising" the distributions by averaging ATDs across 10 consecutive CWs, the distributions reflected characteristics of the response (Fig. 5E, red lines): In the case of the ambient sound, the distribution was double-peaked corresponding to the trough and peak regimes during the main part of the stimulation. In the case of the vocalization, the distribution exhibited a distinct peak accompanied by a "tail" of large ATDs corresponding to the pronounced increase in ATD that occurred during the response to the stimulus.

DISCUSSION

We explored activity-dependent changes in ATD at the calyx of Held in vivo. The dynamics of ATD were quantified at response onset and during recovery. Further, ATDs could be predicted in sequences of events using a phenomenological model. ATD changes were shown to occur under natural

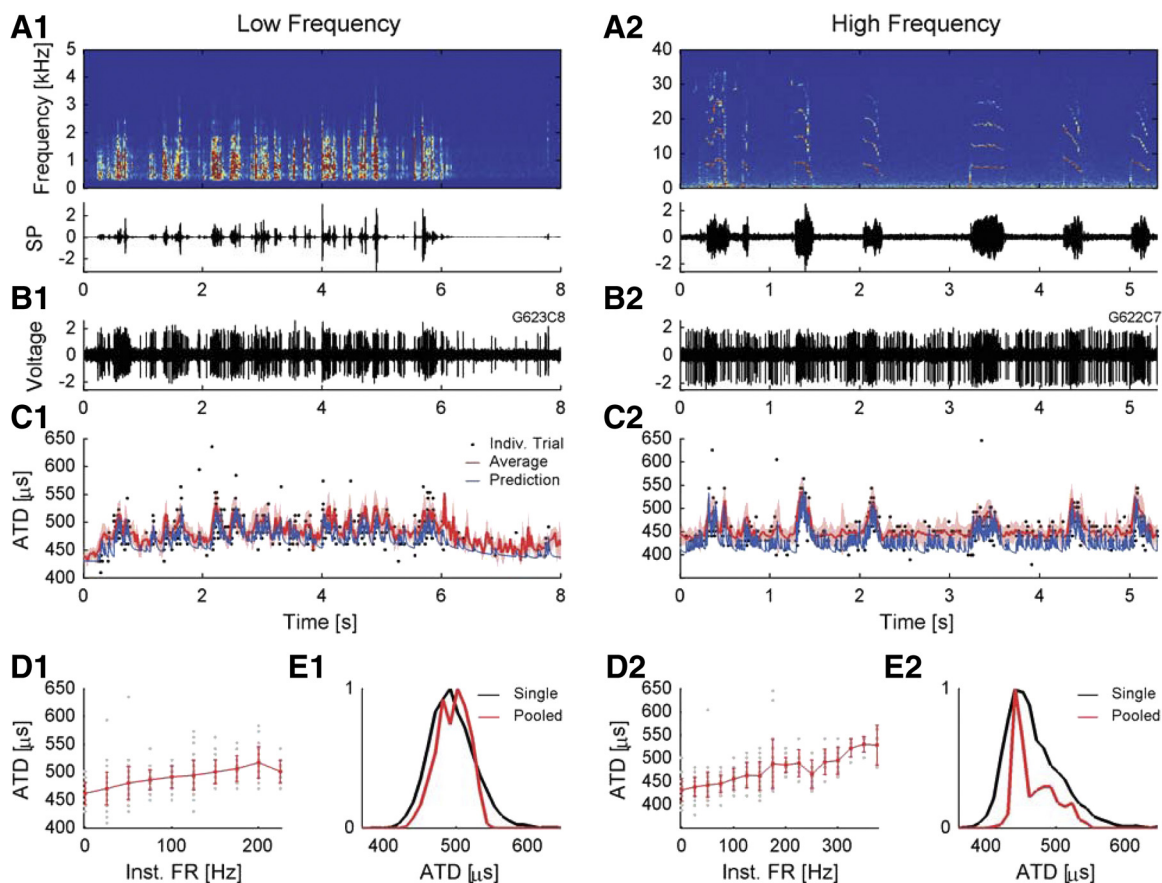


FIG. 5. Changes in ATD in response to natural stimuli. Ambient sounds (left) and gerbil calls (right) were used to examine ATD changes in responses to biologically relevant stimuli. A: spectrogram (top) and stimulus waveform (bottom, sound pressure) of natural stimuli. The ambient sound is dominated by low frequencies, the gerbil calls by high frequencies. B: single units respond with changes in their FR to natural stimuli. C: the ATD changes in correspondence to variations in FR (black dots: single trial; red/pink: mean/SD of 25 trials; blue: model prediction of ATD). The model predictions are matched well to the average ATD values. D: ATD as a function of instantaneous FR exhibits a similar shape as the ATD vs. FR relationship in response to pure tone stimulation (Fig. 2, B and C). The inst. FR was calculated over a 40 ms time window before each action potential. E: distribution of ATDs occurring in response to natural stimuli (black: single ATDs, red: ATDs averaged for 20 transmission events, distribution normalized to peak). The double peak for the averaged ATDs for the low-frequency stimulation (E1, red) is due to the high spontaneous activity of the unit resulting in the lack of small ATDs and 2 regimes of elongated ATDs. On the contrary, the distribution of the averaged ATDs for the high-frequency stimulation (E2, red) is bimodal since both small and high averaged ATDs were present in the response.

stimulation and to share a similar time scale with the maximal interaural time differences experienced by gerbils. Therefore the changes in ATD could be relevant for modeling sound localization.

Definition and interpretation of ATD

ATD was defined as the time between the pre- and the postsynaptic peak of the CW (see also McLaughlin et al. 2008). While the pre- and postsynaptic origins of the CW components have been demonstrated pharmacologically (Haustein et al. 2008; Wu and Kelly 1992b), the exact relation to their underlying intracellular signals are unclear, i.e., transmembrane currents underlying action potentials (APs) and excitatory postsynaptic potentials (EPSPs).

In volume conductor theory, extracellular potentials reflect transmembrane currents, i.e., should be proportional to the derivative of the intracellular voltage (Gold et al. 2006 and references therein; Holt and Koch 1999; Humphrey and Schmidt 1990). Both the positive presynaptic and the first positive postsynaptic CW components are the first and fastest components for the calyx and the postsynaptic cell, respectively. This suggests that each corresponds to the fast rising phase of the pre- and postsynaptic APs, respectively, which should generate the largest transmembrane currents. Because the currents occur simultaneously to the respective changes in intracellular potentials, these two points in time constitute a precise AP transmission time at the synapse.

Another interpretation of the *in vivo* extracellularly recorded CWs comes from *in vitro* loose patch recordings in the same system (Hermann et al. 2007). Under these recording conditions, the cell surface is contacted by the electrode, but no giga seal is formed. This results in signals that share many properties with the present CWs (Fig. 7G in Hermann et al. 2007), first and foremost the two positive peaks, which are also of pre- and postsynaptic origin. Depending on whether the presently analyzed signals are to be interpreted as reflecting intracellular voltages or transmembrane currents, our definition of ATD either captures the time between the maximal pre- and postsynaptic AP voltages or the time between their maximal rises, respectively.

While only a direct comparison between intra- and extracellular recordings can fill in the details of this correspondence, the ATD still provides a precise and quantitatively meaningful measurement of signal transmission delay at the calyx of Held under either of the current interpretations.

Comparison with *in vitro* data

To translate future *in vitro* results into the *in vivo* context, it is worthwhile to compare the estimated properties of the ATD to the corresponding values obtained by Fedchyshyn and Wang (2007). We focus on their 35°C condition, as it comes closest to the *in vivo* situation. A comparison is nontrivial because the ATD does not correspond exactly to the delay up to the peak EPSC and because not exactly the same paradigms and quantities were considered: Fedchyshyn and Wang (2007) estimated the increase per event by linear regression of the measured delays versus event number of a 200 Hz train (30 pulses). Due to the recovery of the delay components in between two events, the estimated increases per event underestimate the actual

values. While exponential models asymptotically predict nonlinear increases in delay, combinations of parameters and stimulation rates exist, which render the initial portion of the ATD change close to linear [note also, that most delay sequences in Fedchyshyn and Wang (2007) showed a slowed increase later in the train, consistent with predictions of the exponential models]. We can compare the two quantities, by considering only the first two events of a train: $\Delta D = \Delta D_{FW} / (1 - e^{-ISI/\tau})$, where ISI denotes the interspike interval (5 ms) and ΔD_{FW} and ΔD represent the delays measured by Fedchyshyn and Wang (2007) or our results, respectively. Here only the fast monoexponential recovery is assumed because it will dominate in the 5 ms ISIs for the 200 Hz stimulation. The present ATD should be the sum of the synaptic delay (SD, 1.1 μ s/event) and the response rise delay (RRD, 1.2 μ s/event), as measured by Fedchyshyn and Wang (2007; p. 589), i.e., 2.3 μ s/event. Using the formula in the preceding text and the present range of τ (15–50 ms, Fig. 4E) translates to a range of A_M of [8.1, 24.2] ms, which corresponds well to the presently estimated range (Fig. 4D).

Concerning the time constants, a comparison is more complicated: the RRD decays monoexponentially ($\tau_{D,mono} = 170$ ms, 1 cell) (Fedchyshyn and Wang 2007), while the SD shows a clearly biexponential decrease ($\tau_{D,fast} = 13$ ms, $\tau_{D,slow} = 1,130$ ms). Depending on the relative amplitudes, the sum of the two processes will appear to behave mono-, bi-, or triexponentially. This amplitude dependence could explain the presently observed partition into mono- and biexponential recoveries.

Mechanisms underlying changes of ATD

Although the present study cannot by itself provide insight into the biophysical underpinning of the increase in ATD, we can relate these *in vivo* measurements to quantities measured in previous *in vitro* studies. Fedchyshyn and Wang (2007) split up the total duration from stimulus onset to the peak of the postsynaptic EPSC into three parts: conduction delay (CD), defined from stimulus onset to the peak of the presynaptic current; SD, from the latter up to the beginning (i.e., maximum curvature) of the postsynaptic EPSC; and RRD, from the latter to the peak of the EPSC. If the interpretation of the extracellularly recorded CWs as the transmembrane currents was correct (see preceding text), then the ATD measured in the present study would correspond to the sum of SD and the time until the steepest ascent of the AP is reached. The latter could be close to RRD or longer, particularly for small EPSCs after short-term depression.

Activity-dependent increases have been observed for both SD and RRD and their dependence on temperature, extracellular Ca^{2+} concentration, and the Ca^{2+} -buffer EGTA has been investigated (Fedchyshyn and Wang 2007). The difference at room temperature versus 35°C had a strong effect on both SD and RRD, reducing each by ~75%. This is more than expected considering recent results on temperature-induced changes in kinetics, e.g., for the postsynaptic AMPA-Rs 30% reduction have been predicted (Postlethwaite et al. 2007). Lowering the extracellular Ca^{2+} concentration or adding the Ca^{2+} -buffer EGTA to the cytosol of the presynaptic terminal led to reductions of similar magnitude, both for SD (45 and 35%) and RRD (35 and 25%). Both effects point to slower usage of a limited

quantity, either slower depletion of the pool of readily releasable vesicles or slower decrease of the release probability (Fedchyshyn and Wang 2007). Together with a high correlation in the respective time courses of recovery, Fedchyshyn and Wang (2007) have concluded that synaptic depression and changes in synaptic delay might be closely related and thus share underlying mechanisms (for review, see Lin and Faber 2002; and also Waldeck et al. 2000; Wu and Borst 1999). Further, heterogeneous distances of active zones to Ca^{2+} channels could lead to increases in ATD. During a sequence of APs, the Ca^{2+} diffusion time from the channels to the active release sites could increase due to the depletion of proximal sites.

Time constants are often more characteristic for the underlying mechanisms than amplitudes. They are in the same range for the recovery from synaptic depression [biexponential, 31 ms and 4.6 s, at 35–37°C (Billups et al. 2005); monoexponential, 90 ms, at 36–37°C (Hermann et al. 2007); monoexponential, 4.2 s, at 21–25°C (von Gersdorff et al. 1997)] and the recovery of ATD. Thus they might point at underlying mechanisms of ATD changes. For the fast process, candidates are the recovery from inactivation of postsynaptic voltage-gated Na^+ channels (biexponential, 1.2 and 125 ms) (Leao et al. 2005) and the recovery from desensitization of the postsynaptic AMPA receptors [monoexponential, ~ 28 ms (Joshi et al. 2004); monoexponential, 21 ms (Taschenberger et al. 2005)]. A candidate mechanism that might underlie the slow time constant is the replenishment of the readily releasable vesicle pool with fast time constants in the sub-second range [84 ms (Wang and Kaczmarek 1998); 200 ms (Wu and Borst 1999); 110 ms (Wu and Wu 2001); 510 ms (Xu and Wu 2005)]. For physiological temperature, this time constants could even be faster. Other processes involved in synaptic depression and recovery thereof seem to have time constants that are too long to be compatible with even the slow time constant of ATD changes, e.g., the recovery from presynaptic inactivation of Ca^{2+} currents (biexponential, 7.5 s and 53 s) (Forsythe et al. 1998).

The simple, phenomenological models used to quantify the dynamics in ATD are not intended to provide a full account of the involved mechanisms. Although a physiology-based model would be preferable, the present understanding of the increase in ATD does not allow a well guided choice. Fedchyshyn and Wang (2007) have hypothesized that the increase in synaptic delay and synaptic depression could reflect the same underlying cause, as they observed both to follow similar time courses. If this hypothesis holds, the presently obtained time constants for ATD changes could be interpretable as their counterparts in synaptic depression (see preceding text and Hennig et al. 2007; Weis et al. 1999).

ATD changes constrain models of sound source localization

As part of the circuits that compute sound source location based on interaural intensity and time differences (IIDs, ITDs), the medial and lateral superior olives (MSO, LSO) receive a monaural glycinergic input from the MNTB (Kuwabara and Zook 1992; Sommer et al. 1993), which is thought to be crucial for the direction selectivity of the neuronal responses (MSO: Brand et al. 2002; LSO: Moore and Caspary 1983). Considering that naturally occurring ITDs in the gerbil are in the range of $\pm 140 \mu\text{s}$ (Maki and Furukawa 2005) and their best localization threshold of 20° corresponds to an ITD of $45 \mu\text{s}$ (Maier and Klump 2006), the magnitude of ATD changes might have constrained the brain's strategies for computing the location of acoustic stimuli.

We illustrate the putative effect of an ATD increase on sound localization by considering a stimulus from the right and the resulting effect on ITD coding in the left MSO (Fig. 6, *inset*). Due to the lack of ATD data at other synapses in the circuit, we assume their ATDs to be constant and only consider the timing between contralateral/inhibitory and ipsilateral/excitatory inputs to the MSO (i.e., ITDs). An increase in ATD at the calyx simply adds to the contralateral delay and would thus decrease the ITD, i.e., the difference in arrival time between contralateral and ipsilateral input ($\text{ITD}_{\Delta\text{ATD}}$, Fig. 6A). A sound localization model that does not compensate for changes in

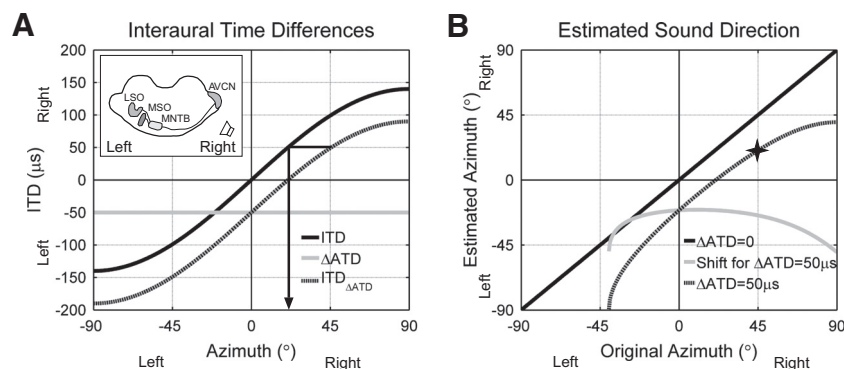


FIG. 6. Influence of ΔATD on a model of signal processing in the left medial and lateral superior olives (MSO/LSO; see *inset*) requiring temporally precise inhibition. *A*: influence on interaural time differences (ITDs). Stimulus positions in the azimuthal plane result in corresponding ITDs of afferent activity. Positions between $\pm 90^\circ$ cause differences ranging between $\pm 140 \mu\text{s}$ for the gerbil (Maki and Furukawa 2005) (solid black). Values are approximated by $\text{ITD} = (d_h \cdot \sin q_s) / v_s$, where d_h denotes the head's diameter, v_s the speed of sound, and q_s the direction of the sound source in the azimuthal plane. An interaural time difference of $0 \mu\text{s}$ encodes the frontal position of a sound. Positive and negative values correspond to right and left positions, respectively. During acoustic stimulation the ATD increases and inhibition arriving via the left MNTB is thus delayed by ΔATD . A ΔATD of $50 \mu\text{s}$ (gray) results in a shift of interaural time differences (solid black) toward $\text{ITD}_{\Delta\text{ATD}}$ (dashed black, arrow). *B*: influence on estimated sound locations. If $\text{ITD}_{\Delta\text{ATD}}$ is used to estimate sound source location by the inverse ITD-location function $q_s = \arcsin(\text{ITD}_{\Delta\text{ATD}} \cdot v_s / d_h)$, predictions are shifted to the left (dashed black) relative to the original location (solid black). The magnitude of this shift depends on the azimuth of the sound source (gray). The prediction can also be made graphically by estimating the $\text{ITD}_{\Delta\text{ATD}}$ value on the ITD curve (black in *A*) and determining its location (arrows in *A*, star in *B*).

ATD would then interpret the resulting $ITD_{\Delta ATD}$ in the left MSO as a sound location further to the left, i.e., at a more ipsilateral position (Fig. 6B, $\Delta ATD = 50 \mu s$).

The effect of ATD changes at the calyx of Held might well be compensated by similar ATD changes at the synapses in the ipsilateral pathway to the MSO. However, the contralateral pathway via the MNTB contains one more synapse, suggesting a larger, total increase in ATD. Unless future measurements indicate a compensation, we would conclude that the observed ATD changes on the inhibitory pathway constrain models of sound source localization in which the exact timing of the inhibitory input is crucial.

ATD variability could limit behavioral performance

In the LSO, the inhibition provided by the MNTB follows closely or even precedes the excitatory input (Joris and Yin 1995). The inhibitory afferents effectively suppress the effect of the excitatory input for up to a few milliseconds (Irvine et al. 2001; Joris and Yin 1995; Park et al. 1996; Sanes 1990; Wu and Kelly 1992a). Not only the amplitude, but also the relative timing between the excitatory and the inhibitory inputs contribute to the IID sensitivity of LSO neurons. Already delays in the range of $\sim 100 \mu s$ can be decisive for spike elicitation (Irvine et al. 2001; Park et al. 1996; Wu and Kelly 1992a). Such delays are equivalent to IIDs that differ on the order of a few decibels (Irvine et al. 2001; Park et al. 1996). Because a 4 dB IID is regarded a sufficient localization cue (8 kHz tone, 30° discrimination threshold) (Maier and Klump 2006), the increase in ATD introduced at the calyx of Held could be determinant for ILD discrimination thresholds.

In the MSO, recent studies provided evidence that the timing and duration of the inhibitory input influence the encoding of ITDs (Brand et al. 2002; Pecka et al. 2008). Changes in ATD should thus have a notable effect on MSO response properties, reflected in an ipsilateral shift in the MSO ITD preference for different response rates. Pecka et al. (2008) measured ITD preference for different stimulus intensities (and consequently response rates) and found only mild ipsilateral shifts of ITD preference. However, a ΔATD -induced shift would be expected to occur only in the limited range of sound intensities corresponding to the steep part of the rate-intensity function. Only $\sim 2\text{--}5 \mu s/dB$ would be expected from the range of presently observed $\Delta ATDs$. If the ITD preference was independent of response rate, other compensatory mechanisms need to be considered, e.g., similar changes in ATD could apply to the excitatory pathways to the MSO, or the presence of inhibition already suffices for determining the ITD preference, as proposed in a recent model of MSO processing (Zhou et al. 2005).

As demonstrated in the present study, the increase in ATD exhibits a positive correlation with CF. Considering that the MNTB's target nuclei also differ in their CF distribution - MSO neurons have mostly low CFs (Inbody and Feng 1981), LSO neurons a bias to higher CFs (Guinan et al. 1972; Tsuchitani 1977)—this CF dependence could correspond to the required precision in low- and high-frequency sound localization.

While previous studies led to the understanding that at the calyx of Held “the delays have an extremely low variability or ‘jitter’ in their timing” (von Gersdorff and Borst 2002), vari-

ability of ATD seems to be a robust phenomenon in vivo and in vitro. This renders it promising to study the ATD at other central synapses, a view which is supported by similar findings in other systems (Swandulla et al. 1991; Vyshedskiy et al. 2000; Waldeck et al. 2000).

ACKNOWLEDGMENTS

We thank M. Typlt and R. Stollhoff for useful discussions and the anonymous reviewers for valuable comments.

Present address of S. Tolnai: Dept. of Physiology, Anatomy and Genetics, University of Oxford, Oxford OX1 3PT, United Kingdom.

GRANTS

Financial support was provided by the DFG to R. Rübsamen (Ru 390-18/1). B. Englitz and S. Tolnai were supported by the Graduate Program INTERNEURO (GRK 1097) at the University of Leipzig.

REFERENCES

- Barrett EF, Stevens CF.** The kinetics of transmitter release at the frog neuromuscular junction. *J Physiol* 227: 691–708, 1972.
- Billups B, Graham BP, Wong AY, Forsythe ID.** Unmasking group III metabotropic glutamate autoreceptor function at excitatory synapses in the rat CNS. *J Physiol* 565: 885–896, 2005.
- Borst JG, Helmchen F, Sakmann B.** Pre- and postsynaptic whole-cell recordings in the medial nucleus of the trapezoid body of the rat. *J Physiol* 489: 825–840, 1995.
- Brand A, Behrend O, Marquardt T, McAlpine D, Grothe B.** Precise inhibition is essential for microsecond interaural time difference coding. *Nature* 417: 543–547, 2002.
- Fedchyshyn MJ, Wang LY.** Activity-dependent changes in temporal components of neurotransmission at the juvenile mouse calyx of Held synapse. *J Physiol* 581: 581–602, 2007.
- Forsythe ID.** Direct patch recording from identified presynaptic terminals mediating glutamatergic EPSCs in the rat CNS in vitro. *J Physiol* 479: 381–387, 1994.
- Forsythe ID, Tsujimoto T, Barnes-Davies M, Cuttle MF, Takahashi T.** Inactivation of presynaptic calcium current contributes to synaptic depression at a fast central synapse. *Neuron* 20: 797–807, 1998.
- Gold C, Henze DA, Koch C, Buzsáki G.** On the origin of the extracellular action potential waveform: a modeling study. *J Neurophysiol* 95: 3113–3128, 2006.
- Guinan JJ Jr, Li RY.** Signal processing in brain stem auditory neurons which receive giant endings (calyces of Held) in the medial nucleus of the trapezoid body of the cat. *Hear Res* 49: 321–334, 1990.
- Guinan JJ Jr, Norris, BE Guinan, SS.** Single auditory units in the superior olivary complex. II. Locations of unit categories and tonotopic organization. *Int J Neurosci* 4: 147–166, 1972.
- Haustein MD, Reinert T, Warnatsch A, Englitz B, Dietz B, Robitzki A, Rübsamen R, Milenkovic I.** Synaptic transmission and short-term plasticity at the calyx of Held synapse revealed by multielectrode array recordings. *J Neurosci Methods* 174: 227–236, 2008.
- Held H.** Die zentrale Gehörleitung. In: *Archiv für Anatomie und Physiologie*, edited by His W, Du Bois-Reymond E. Leipzig: Leipzig Verlag von Veit und Comp, 1893, p. 201–380.
- Hennig MH, Postlethwaite M, Forsythe ID, Graham BP.** A biophysical model of short-term plasticity at the calyx of Held. *Neurocomputing* 70: 1626–1629, 2007.
- Hennig MH, Postlethwaite M, Forsythe ID, Graham BP.** Interactions between multiple sources of short-term plasticity during evoked and spontaneous activity at the rat calyx of Held. *J Physiol* 586: 3129–3146, 2008.
- Hermann J, Pecka M, von Gersdorff H, Grothe B, Klug A.** Synaptic transmission at the calyx of Held under in vivo like activity levels. *J Neurophysiol* 98: 807–820, 2007.
- Holt GR, Koch C.** Electrical interactions via the extracellular potential near cell bodies. *J Comput Neurosci* 6: 169–184, 1999.
- Humphrey DR, Schmidt EM.** Extracellular single-unit recording methods. In: *Neurophysiological Techniques: Applications to Neural Systems*, edited by Boulton AA, Baker GB, Vanderwolf CH. Clifton, NJ: Humana, 1990, p. 1–64.
- Inbody SB, Feng AS.** Binaural response characteristics of single neurons in the medial superior olivary nucleus of the albino rat. *Brain Res* 210: 361–366, 1981.

- Irvine DR, Park VN, McCormick L.** Mechanisms underlying the sensitivity of neurons in the lateral superior olive to interaural intensity differences. *J Neurophysiol* 86: 2647–2666, 2001.
- Joris PX, Yin TC.** Envelope coding in the lateral superior olive. I. Sensitivity to interaural time differences. *J Neurophysiol* 73: 1043–1062, 1995.
- Joshi I, Shokralla S, Titis P, Wang LY.** The role of AMPA receptor gating in the development of high-fidelity neurotransmission at the calyx of Held synapse. *J Neurosci* 24: 183–196, 2004.
- Katz B, Miledi R.** The measurement of synaptic delay, and the time course of acetylcholine release at the neuromuscular junction. *Proc R Soc Lond B Biol Sci* 161: 483–495, 1965.
- Kopp-Scheinflug C, Lippe WR, Dorrscheidt GJ, Rubsamen R.** The medial nucleus of the trapezoid body in the gerbil is more than a relay: comparison of pre- and postsynaptic activity. *J Assoc Res Otolaryngol* 4: 1–23, 2003.
- Kuwabara N, Zook JM.** Projections to the medial superior olive from the medial and lateral nuclei of the trapezoid body in rodents and bats. *J Comp Neurol* 324: 522–538, 1992.
- Leao RM, Kushmerick C, Pinaud R, Renden R, Li GL, Taschenberger H, Spiro G, Levinson SR, von Gersdorff H.** Presynaptic Na⁺ channels: locus, development, and recovery from inactivation at a high-fidelity synapse. *J Neurosci* 25: 3724–3738, 2005.
- Lin JW, Faber DS.** Modulation of synaptic delay during synaptic plasticity. *Trends Neurosci* 25: 449–455, 2002.
- Maier JK, Klump GM.** Resolution in azimuth sound localization in the Mongolian gerbil (*Meriones unguiculatus*). *J Acoust Soc Am* 119: 1029–1036, 2006.
- Maki K, Furukawa S.** Acoustical cues for sound localization by the Mongolian gerbil, *Meriones unguiculatus*. *J Acoust Soc Am* 118: 872–886, 2005.
- McLaughlin M, van der Heijden M, Joris PX.** How secure is in vivo synaptic transmission at the calyx of Held? *J Neurosci* 28: 10206–10219, 2008.
- Moore MJ, Caspary DM.** Strychnine blocks binaural inhibition in lateral superior olivary neurons. *J Neurosci* 3: 237–242, 1983.
- Morest DK.** The growth of synaptic endings in the mammalian brain: a study of the calyces of the trapezoid body. *Z Anat Entwicklungsgesch* 127: 201–220, 1968.
- Park TJ, Grothe B, Pollak GD, Schuller G, Koch U.** Neural delays shape selectivity to interaural intensity differences in the lateral superior olive. *J Neurosci* 16: 6554–6566, 1996.
- Pecka M, Brand A, Behrend O, Grothe B.** Interaural time difference processing in the mammalian medial superior olive: the role of glycinergic inhibition. *J Neurosci* 28: 6914–6925, 2008.
- Postlethwaite M, Hennig MH, Steinert JR, Graham BP, Forsythe ID.** Acceleration of AMPA receptor kinetics underlies temperature-dependent changes in synaptic strength at the rat calyx of Held. *J Physiol* 579: 69–84, 2007.
- Sanes DH.** An in vitro analysis of sound localization mechanisms in the gerbil lateral superior olive. *J Neurosci* 10: 3494–3506, 1990.
- Schneggenburger R, Forsythe ID.** The calyx of Held. *Cell Tissue Res* 326: 311–337, 2006.
- Schwarz G.** Estimating the dimensions of a model. *Ann Stat* 6: 461–464, 1978.
- Sommer I, Lingenhohl K, Friauf E.** Principal cells of the rat medial nucleus of the trapezoid body: an intracellular in vivo study of their physiology and morphology. *Exp Brain Res* 95: 223–239, 1993.
- Swandulla D, Hans M, Zipser K, Augustine GJ.** Role of residual calcium in synaptic depression and posttetanic potentiation: fast and slow calcium signaling in nerve terminals. *Neuron* 7: 915–926, 1991.
- Taschenberger H, Scheuss V, Neher E.** Release kinetics, quantal parameters and their modulation during short-term depression at a developing synapse in the rat CNS. *J Physiol* 568: 513–537, 2005.
- Tsuchitani C.** Functional organization of lateral cell groups of cat superior olivary complex. *J Neurophysiol* 40: 296–318, 1977.
- von Gersdorff H, Borst JG.** Short-term plasticity at the calyx of held. *Nat Rev Neurosci* 3: 53–64, 2002.
- von Gersdorff H, Schneggenburger R, Weis S, Neher E.** Presynaptic depression at a calyx synapse: the small contribution of metabotropic glutamate receptors. *J Neurosci* 17: 8137–8146, 1997.
- Vyshedskiy A, Allana T, Lin JW.** Analysis of presynaptic Ca²⁺ influx and transmitter release kinetics during facilitation at the inhibitor of the crayfish neuromuscular junction. *J Neurosci* 20: 6326–6332, 2000.
- Waldeck RF, Pereda A, Faber DS.** Properties and plasticity of paired-pulse depression at a central synapse. *J Neurosci* 20: 5312–5320, 2000.
- Wang LY, Kaczmarek LK.** High-frequency firing helps replenish the readily releasable pool of synaptic vesicles. *Nature* 394: 384–388, 1998.
- Weis S, Schneggenburger R, Neher E.** Properties of a model of Ca(2+)-dependent vesicle pool dynamics and short term synaptic depression. *Biophys J* 77: 2418–2429, 1999.
- Wu LG, Borst JG.** The reduced release probability of releasable vesicles during recovery from short-term synaptic depression. *Neuron* 23: 821–832, 1999.
- Wu SH, Kelly JB.** Binaural interaction in the lateral superior olive: time difference sensitivity studied in mouse brain slice. *J Neurophysiol* 68: 1151–1159, 1992a.
- Wu SH, Kelly JB.** Synaptic pharmacology of the superior olivary complex studied in mouse brain slice. *J Neurosci* 12: 3084–3097, 1992b.
- Wu XS, Wu LG.** Protein kinase C increases the apparent affinity of the release machinery to Ca²⁺ by enhancing the release machinery downstream of the Ca²⁺ sensor. *J Neurosci* 21: 7928–7936, 2001.
- Xu J, Wu LG.** The decrease in the presynaptic calcium current is a major cause of short-term depression at a calyx-type synapse. *Neuron* 46: 633–645, 2005.
- Zhou Y, Carney LH, Colburn HS.** A model for interaural time difference sensitivity in the medial superior olive: interaction of excitatory and inhibitory synaptic inputs, channel dynamics, and cellular morphology. *J Neurosci* 25: 3046–3058, 2005.